Hindawi
Adsorption Science & Technology
Volume 2023, Article ID 1829725, 16 pages
https://doi.org/10.1155/2023/1829725

Research Article

Nanoscale Zero-Valent Iron Dispersed by Sodium Alginate Enables Highly Efficient Removal of Lead (Pb) from Aqueous Solution

Chunli Zheng,[1] **Jieling Ren**,[1] **Fei He**,[1] **Yingying Yong**,[1] **Yanhong Tu**,[2] **and Zhenxing Wang**[3]

[1]*Department of Environmental Science and Engineering, Xi'an Jiaotong University, Xi'an 710049, China*
[2]*Xingzhi College Zhejiang Normal University, Lanxi 321100, China*
[3]*Environmental Protection Key Laboratory of Environmental Pollution Health Risk Assessment, South China Institute of Environmental Sciences, MEE, Guangzhou 510655, China*

Correspondence should be addressed to Yanhong Tu; tuyanhong130815@163.com and Zhenxing Wang; 271886581@qq.com

Received 30 December 2022; Revised 25 May 2023; Accepted 8 June 2023; Published 23 June 2023

Academic Editor: Nguyen Hai Tran

Nanozero-valent iron (NZVI) shows great potential in the remediation of water pollution, but its application is limited by its instability and tendency to aggregate. To enhance the dispersibility and antioxidant properties of NZVI, we prepared composites (SN) by wrapping NZVI with sodium alginate (SA) for the removal of Pb(II) from water. Various characterization methods such as SEM-EDS, BET, XPS, and FT-IR were used to study the structure of the materials, and the adsorption properties of Pb(II) in the materials were analyzed using adsorption kinetics and adsorption isotherm experiments. The results showed that SN had a specific surface area of 47.05 m^2/g, which was significantly higher than the 7.56 m^2/g of NZVI, and the surface passivation was reduced. The maximum adsorption amount of SN on Pb(II) was obtained by fitting the adsorption isotherm model at 70.92 mg/g. After five cycles of adsorption, SN exhibited a removal rate of 95.11% for Pb(II). The mechanism of Pb(II) removal by SN involved the synergistic effect of electrostatic adsorption, redox reaction, ion exchange, and coprecipitation. Notably, even after 90 days of aging, the removal rate of Pb(II) by SN remained high at 95.39%, demonstrating good reactivity. These results indicated that SN is an effective adsorbent to remove Pb(II) contamination.

1. Introduction

Lead (Pb) is one of the most hazardous heavy metals that is caused primarily by anthropogenic activities, including battery manufacturers, lead-based paints, mine drainage, phosphate fertilizers, lead smelting, and the ammunition industry [1]. Pb is a nonessential element of organisms, once absorbed by humans, which would cause serious damage to the human mental health, hematopoietic system, and kidney even in low concentrations [2]. Therefore, it is imperative to identify an appropriate remediation technology capable of removing Pb(II) from wastewater.

Currently, the main removal methods of Pb(II) from wastewater include adsorption, precipitation, liquid-liquid extraction, and ion exchange, [3, 4]. Amongst these, adsorption is proven to be one of the most effective remediation techniques with simple, high effectiveness, and economical cost [5, 6]. Over the last few years, various types of adsorbents are developed for the removal of heavy metals from wastewater (e.g., biochar, sepiolite, organic fertilizer, as well as nanobiorepair materials) [7–10]. In particular, nanoscale zero-valent iron (NZVI) has emerged as one of the most effective materials due to its abundant active sites and reductive removal capacity of heavy metals [11, 12]. However, NZVI is easy to form aggregates under van der Waals and magnetic force, which will lead to the reduction in remediation efficiency [13, 14]. Therefore, there is a need to develop effective ways to ensure the stability and remediate efficiency of NZVI.

Sodium alginate (SA), a linear polysaccharide with a lot of free carboxyl groups, is commonly used to remediate heavy metals [15]. Previous studies have reported that SA could form stable hydrogels with some cations (such as Ca^{2+} and Fe^{3+}) [16, 17]. Yu et al. [18] found that SA, a predominant dispersant, can improve the immobilization of biological enzymes by nanomaterials. Recently, modifications of NZVI with SA are used for wastewater remediation. Li et al. [19] found SA can improve the penetration and removal rate of chromium removal by NZVI. However, the remediation rate for Pb removal by NZVI with SA is unclear.

The objectives of this study are to prepare an inexpensive and effective NZVI material wrapped by SA and explore the removal effect of modified NZVI on Pb(II) from the aqueous solution. Specifically, the aim was to investigate the immobilization mechanism of the modified materials on Pb by kinetics and structure analysis. On this basis, the effect of different factors on the adsorption of Cd by modified materials was discussed. The results of this study will help remediate Pb(II) from wastewater.

2. Methods and Materials

2.1. Chemicals and Materials. Sodium alginate (SA), calcium chloride ($CaCl_2$), ferric chloride hexahydrate ($FeCl_3{\cdot}6H_2O$), sodium borohydride ($NaBH_4$), anhydrous ethanol, nitric acid (HNO_3), sodium hydroxide (NaOH), and lead nitrate ($Pb(NO_3)_2$) were obtained from the Sinopharm Chemical Reagent. All chemicals were of analytical grade and did not require further purification before use. All solutions were prepared with Milli-Q ultrapure water, and the purity of N_2 used was 99.9%.

2.2. Preparation of NZVI Sample. The preparation of nanozero-valent iron was carried out by modifying the synthetic procedures reported by Lakkaboyana et al. and Wang et al. [20, 21]. Nanozero-valent iron particles were synthesized according to the following steps: (1) 4.88 g of ferric chloride hexahydrate ($FeCl_3{\cdot}6H_2O$) was dissolved in 50 mL of a 30 wt% ethanol solution, then added the prepared solution into a three-necked flask and stirred with N_2 for 30 min to remove the dissolved oxygen in the solution. (2) 3.50 g of $NaBH_4$ was dissolved in 70 mL of deoxygenated deionized water and then sealed up. Then drip the $NaBH_4$ solution into the deoxygenated ferric chloride solution placed in a three-neck flask at a rate of 2 mL/min, and the $NaBH_4$ solution was stirred continuously at a speed of 800 rpm for 30 min by a mechanical stirring device. (3) The prepared black particles were separated by magnet and washed three times with deoxygenated deionized water and absolute ethanol then dried at -60°C for 24 h using a vacuum freeze dryer. After drying, nanosized zero-valent iron (NZVI) was obtained and stored in a vacuum bag.

2.3. Preparation of SN Composite Absorbent. 0.50 g of SA was dissolved in 25 mL of deoxygenated deionized water and mixed for 1.5 h with a magnetic stirrer until the solution was evenly mixed. After mixing, the SA solution was stood for 30 min. Then, the NZVI particles (0.25, 0.33, 0.50, 0.75, and 1.00 g) were rapidly added to the SA solution and stirred evenly with a mechanical stirring device at a speed of 800 rpm. A $CaCl_2$ solution was prepared by adding 4.00 g of $CaCl_2$ particles to 100 mL of deoxygenated deionized water under the N_2 atmosphere for 30 min. The mixture of ZNVI and SA was added drop by drop into the prepared $CaCl_2$ solution with a syringe and passed into high pure N_2 for 3 h. After three cycles of washing with deoxygenated deionized water and absolute ethanol, the gel particles were dried at -60°C for 24 h with a vacuum freeze dryer. After drying, nanozero-valent iron gel particles (SN) were obtained and stored in a vacuum bag.

2.4. Materials Characterizations. To identify the different composite absorbers, the samples were scanned by scanning electron microscopy (SEM, SU5000), energy dispersive spectroscopy (EDS, SU5000), and X-ray diffraction (XRD, D8 Advanced) to show the structure and morphology of the different composite absorbers. In addition, the composite absorbers were identified by Brunauer-Emmett-Teller to analyse their specific surface area and pore structure characteristics and by Fourier transform infrared spectroscopy (FT-IR, Tensor37) to analyse the oxidation state of Fe and Pb. X-ray photoelectron spectroscopy (XPS, Ultim Max) was performed on Ultim Max with an Al Kα emitter to examine changes in material surface composition and chemical state.

2.5. Batch Experiments

2.5.1. Adsorption Kinetic Experiments. Adsorption kinetic experiments of Pb(II) (10 mg/L) by SA, NZVI, and SN (0.10 g) were conducted by shaking at 180 rpm (25°C). The initial pH of composite absorbents and Pb(II) solutions was adjusted to 5.0 ± 0.1 using HNO_3 and NaOH solutions. Samples were taken at different time intervals between 0 and 330 min and then passed through a 0.45 μm PTEE membrane to monitor the Pb(II) contents and pH changes. The concentration of Pb(II) was analysed by an atomic absorption spectrophotometer. All the adsorption experiments were performed three times, and the average values were recorded. Equations (1) and (2) were used to calculate the adsorption capacity q_t (mg/g) and adsorption efficiency w for Pb(II) by three adsorbents.

$$q_t = \frac{(C_0 - C)}{m} \times V, \tag{1}$$

$$w = \frac{(C_0 - C)}{C_0} \times 100\%, \tag{2}$$

where C_0 is the initial Pb(II) concentration (mg/L), C is the residual Pb(II) concentration in solution after adsorption (mg/L), V is the solution volume (L), m is the mass of adsorbent (g), and q_t is the adsorption concentration of Pb(II) on adsorbent at time t (mg/g).

In addition, the first-order kinetic model (3), the second-order kinetic model (4), and the Weber-Morris particle internal diffusion model (5) were used to calculate the relevant kinetic parameters.

$$\ln\left(q_{e,\exp} - q_t\right) = \ln\left(q_{e,\mathrm{cal}}\right) - K_1 t, \quad (3)$$

$$\frac{t}{q_t} = \frac{1}{K_2 q_{e,\mathrm{cal}}^2} + \frac{1}{q_{e,\mathrm{cal}}} t, \quad (4)$$

$$q_t = K_{id} t^{1/2} + I, \quad (5)$$

where q_t is the adsorption concentration of Pb(II) on adsorbent at time t (mg/g); $q_{e,\exp}$ is an experimental measurement value of Pb(II) adsorption capacity on adsorbent at equilibrium time (mg/g); $q_{e,\mathrm{cal}}$ is the calculated value of Pb(II) adsorption capacity on adsorbent at equilibrium time (mg/g); K_1 is the pseudo-first-order adsorption rate constant (1/min); K_2 is pseudo-second-order adsorption rate constant (g/(mg·min)); K_{id} is inparticle diffusion model rate constant (mg/(g·min$^{1/2}$)); and I is intercept (mg/g).

2.5.2. Adsorption Thermodynamic Experiments. In adsorption thermodynamics, add 0.10 g of SA, NZVI, and SN to 50 mL of Pb(II) with varying initial concentrations (5, 10, 30, 50, 100, and 200 mg/L). Then the pH of the mixed solutions was adjusted to 5.0 ± 0.1 using HNO_3 and NaOH solutions. The solution was stirred at 180 rpm in a constant-temperature oscillation box at 25°C. Measure the Pb(II) mass concentration in the supernatant after filtering the samples through a 0.45 μm membrane when the adsorption reaches an equilibrium time of 330 min. All adsorption experiments are performed three times, with the average value recorded. Finally, Langmuir (6) and Freundlich (7) models were used to calculate the adsorption isothermic parameters.

$$q_e = \frac{q_m K_L C_e}{1 + K_L C_e}, \quad (6)$$

$$q_e = K_F C_e^{1/n}, \quad (7)$$

where C_e is the adsorption concentration of Pb(II) remaining in the solution after equilibration (mg/L); q_e is the adsorption concentration of adsorbent to Pb(II) (mg/g); q_m is the maximum adsorption concentration of the adsorbent to Pb(II) (mg/g); K_L is the Langmuir model constant (L/mg); K_F is the Freundlich model constant (mg·(L$^{(1-1/n)}$/g)); and $1/n$ is the Freundlich model constant, which indicates heterogeneity factors.

2.5.3. Recycle Adsorption Experiments. The experimental steps for the adsorption-desorption cycle of an equal amount of sample were as follows:

Transfer 0.10 g of SN or NZVI to a 50 mL conical flask containing 10 mg/L Pb(II) solution and adjust the pH of the mixture to 5.0 ± 0.1 using HNO_3 and NaOH. The solution was stirred at 180 rpm in a constant-temperature oscillation box at 25°C. The mass concentration of Pb(II) in the supernatant was determined by sampling at different time intervals ranging from 0 to 330 min, employing a 10 mL syringe and subsequently filtering the sampled solution through a 0.45 μm membrane. At the same time, the solution in the conical flask was slowly poured out, filtered through quantitative filter paper, and rinsed with ultrapure water until no Pb(II) was detected in the filtrate. The cleaned SN or NZVI was dried through a freeze dryer for 24 h. The above operation was repeated four times with 0.10 g of dried SN or NZVI, and the change in the removal capacity of the samples for Pb(II) was recorded. All the adsorption experiments were performed three times, and the average values were recorded. Equations (1) and (2) were used to calculate the adsorption capacity q_t (mg/g) and adsorption efficiency w for Pb(II) by three adsorbents.

The experimental steps of the adsorption-desorption cycle considering the material mass loss factor were as follows:

The experimental steps for the concentration and detection of Pb(II) in solution and the collection of SN or NZVI solids were consistent with the recycle adsorption procedure for an equal amount of samples. Except for the SN or NZVI remaining after drying, the sample was repeatedly circulated four times to record the change in the removal ability of Pb(II) by the sample and the change in the remaining mass of the sample. All the adsorption experiments were performed three times, and the average values were recorded. Equations (1) and (2) were used to calculate the adsorption capacity q_t (mg/g) and adsorption efficiency w for Pb(II) by three adsorbents.

2.5.4. Aging Experiment of SN. In order to evaluate the stability of the composite, SN and NZVI were stored in a constant temperature and humidity incubator (air, 15°C, 45% relative humidity). The same amount of sample was taken at 1, 30, and 90 d for XRD and XPS characterization, respectively. Meanwhile, the same amount of sample is taken on days 1, 5, 10, 30, and 90 to assess its ability to remove Pb(II). The steps of the adsorption experiment are as follows: 50 mL of Pb(II) solution with 0.10 g of SN granules (NZVI powder) were mixed in 250 mL Erlenmeyer flasks. The pH of the resulting mixture was then carefully adjusted to 5.0 (±0.1) using either NaOH or HNO_3 solutions. Place the Erlenmeyer flask at 180 rpm in a thermostatic shaker at 25°C. Samples were taken with a 10 mL syringe at different time intervals between 0 and 330 min and then passed through a 0.45 μm membrane. The collected filtrate is analysed by an atomic flame atomic absorption spectrophotometer for the concentration of Pb(II). All adsorption experiments are performed three times, with the average value recorded. Equations (1) and (2) were used to calculate the adsorption capacity q_t (mg/g) and adsorption efficiency w of the three adsorbents against Pb(II).

2.6. Analysis Method. The residual concentration of Pb(II) was analysed by atomic absorption spectroscopy (AAS) (WYA2300, China).

3. Results and Discussion

3.1. Structure and Morphologies of Composite Absorbents. As observed in Figures 1(a) and 1(b), the composite adsorbent SN was a black granular substance with a rich pore structure (0.10-0.19 mm). The SN particles investigated in this study

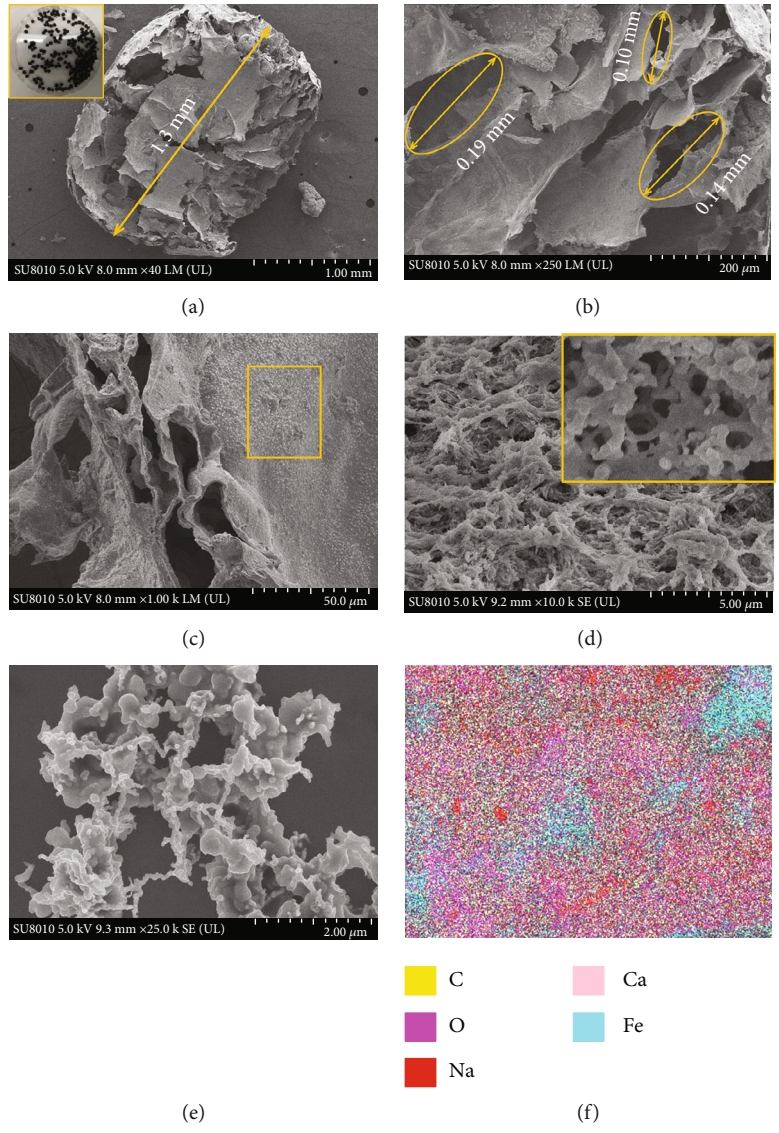

Figure 1: (a–d) SEM images of SN; (e) SEM images of NZVI; (f) EDS elemental analysis of SN.

exhibited a highly porous structure, which promoted the diffusion of pollutants within the material and offered an increased specific surface area for adsorption. Furthermore, examination of the interior of the SN particles revealed the presence of irregularities such as folds and bulges on the surface (Figure 1(c)). Compared with the aggregated NZVI (Figure 1(e)), the NZVI particles in SN were dispersed on the surface and well integrated with the SA matrix, which was attributed to the cross-linking effect of Ca^{2+} on SA (Figure 1(d)). Further analysis of EDS elements showed that the main elements of SN adsorbent spheres included C, O, Na, Ca, and Fe, indicating that NZVI was successfully encapsulated in the SA gel skeleton (Figure 1(f)).

Figures 2(a)–2(c) show the N_2 adsorption-desorption curves of SN, NZVI, and SA. SN and SA exhibited the reversible type IV isotherm characteristic of H_3-type hysteresis lines, indicating the existence of a multilevel pore structure of the material [22]. Pore-size distribution curves further confirmed that SN and SA were rich in micropores and mesopores (Figure 2(d)). Based on the BET and Barrett-Joyner-Halenda (BJH) methods [23], the specific surface area of SA was 8 m^2/g, while that of SN increased to 47 m^2/g, probably owing to the rougher surface provided by the loading of NZVI. In addition, the specific surface area of SN was about 7 times higher than that of NZVI, the microporous pore volume increased by 5 times, and the average pore size decreased by 3 times, which indicated that wrapping NZVI in SA was beneficial to its dispersion and could effectively solve the agglomeration problem of NZVI.

The XRD patterns of SA, NZVI, and SN are shown in Figure 3(a). The characteristic peaks of SN at $2\theta = 44.6^\circ$ and 82.3° were ascribed to the crystal plane diffraction peaks of α-Fe^0(110) and α-Fe^0(211), which indicated the successful complexation of NZVI with SA. The series of characteristic peaks of NZVI at $2\theta = 20.7^\circ$, 26.2°, and 30.3° represented the generation of iron oxide (Fe_3O_4 or γ-Fe_2O_3), indicating

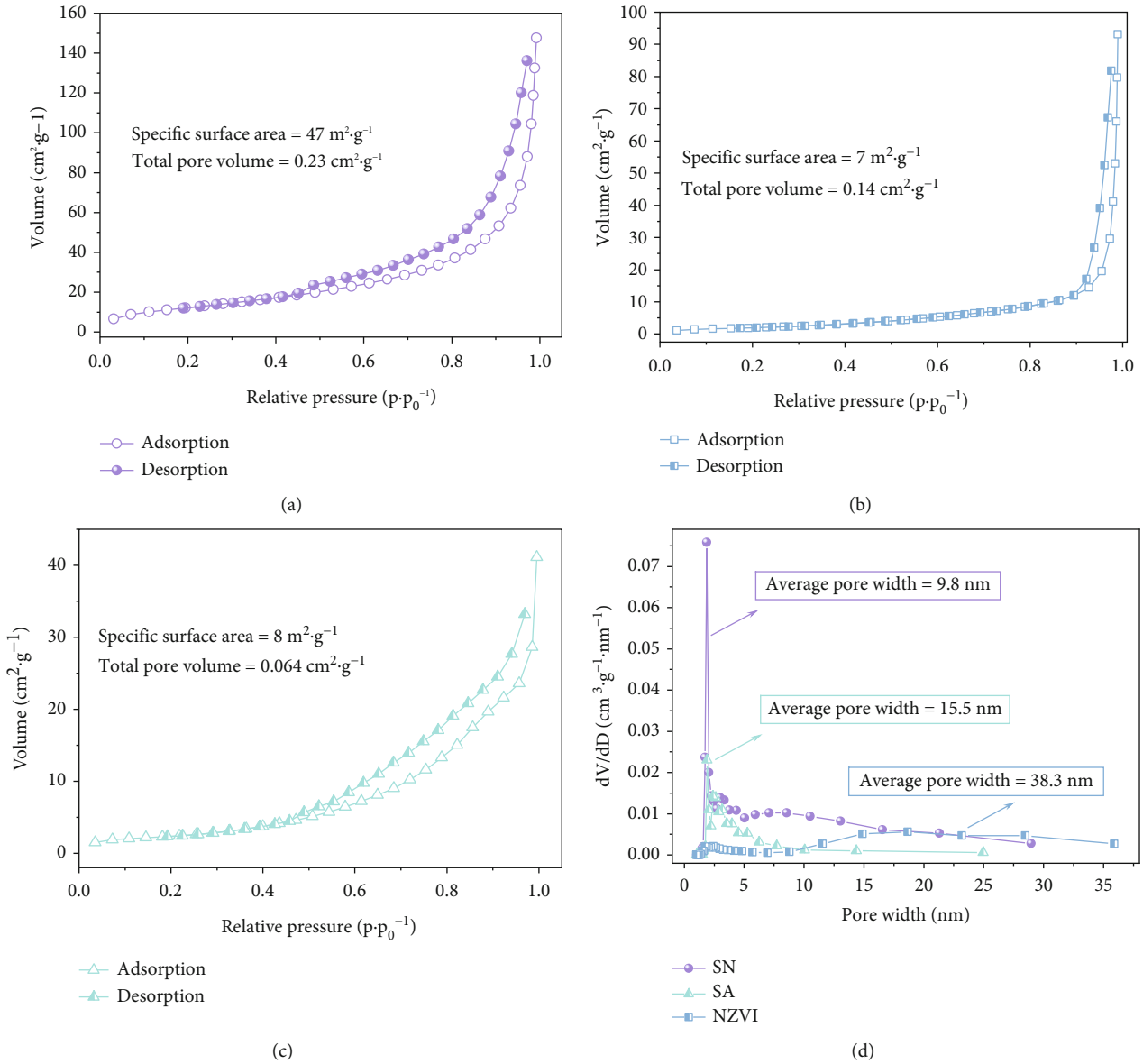

Figure 2: N_2 adsorption-desorption curves of (a) SN, (b) NZVI, (c) SA, and (d) pore-size distribution curve.

the oxidation of NZVI, while the above characteristic peaks were not found in SN, suggesting that the encapsulation of NZVI within SA effectively prevents its oxidation.

To further investigate the functional group properties of the samples, FT-IR spectra of SN, NZVI, and SA were recorded within 400-4000 cm^{-1} of the lattice vibration. As shown in Figure 3(b), all three materials showed vibrational bands attributed to hydroxyl groups at 3500-3900 cm^{-1}, with SA showing a weak broad burr band at 3500-3900 cm^{-1} and SN showing a weak absorption band in the region of 3700-3900 cm^{-1}, where the vibrations of the region are mainly associated with the antisymmetric and symmetric stretching vibrations of the trace liquid H_2O in the gel material and the stretching vibration-rotation band of the gaseous H_2O [24]. The characteristic band of NZVI at 3720 cm^{-1} was ascribed to the vibrational rotation spectrum of gaseous H_2O, while the characteristic band with a wider band range and higher vibrational intensity present near 3124 cm^{-1} is associated with hydroxyl stretching vibration [25]. In addition, the spectral bands associated with the antisymmetric and symmetric stretching vibrations of the carboxy-functional group appeared at 1619 cm^{-1} and 1423 cm^{-1} for SA [26]. While the corresponding characteristic bands for SN appeared at 1626 cm^{-1} and 1415 cm^{-1}, which was probably attributed to the change in the vibrational position of the carboxy-functional group due to the embedding of NZVI.

3.2. Analysis of the Removal Effect of SN on Pb(II). Figure 4 shows the variation curves of the adsorption amounts of Pb(II) on SN, NZVI, and SA at different contact times for an initial concentration of 10 mg/L. Stage 1 shows the rapid

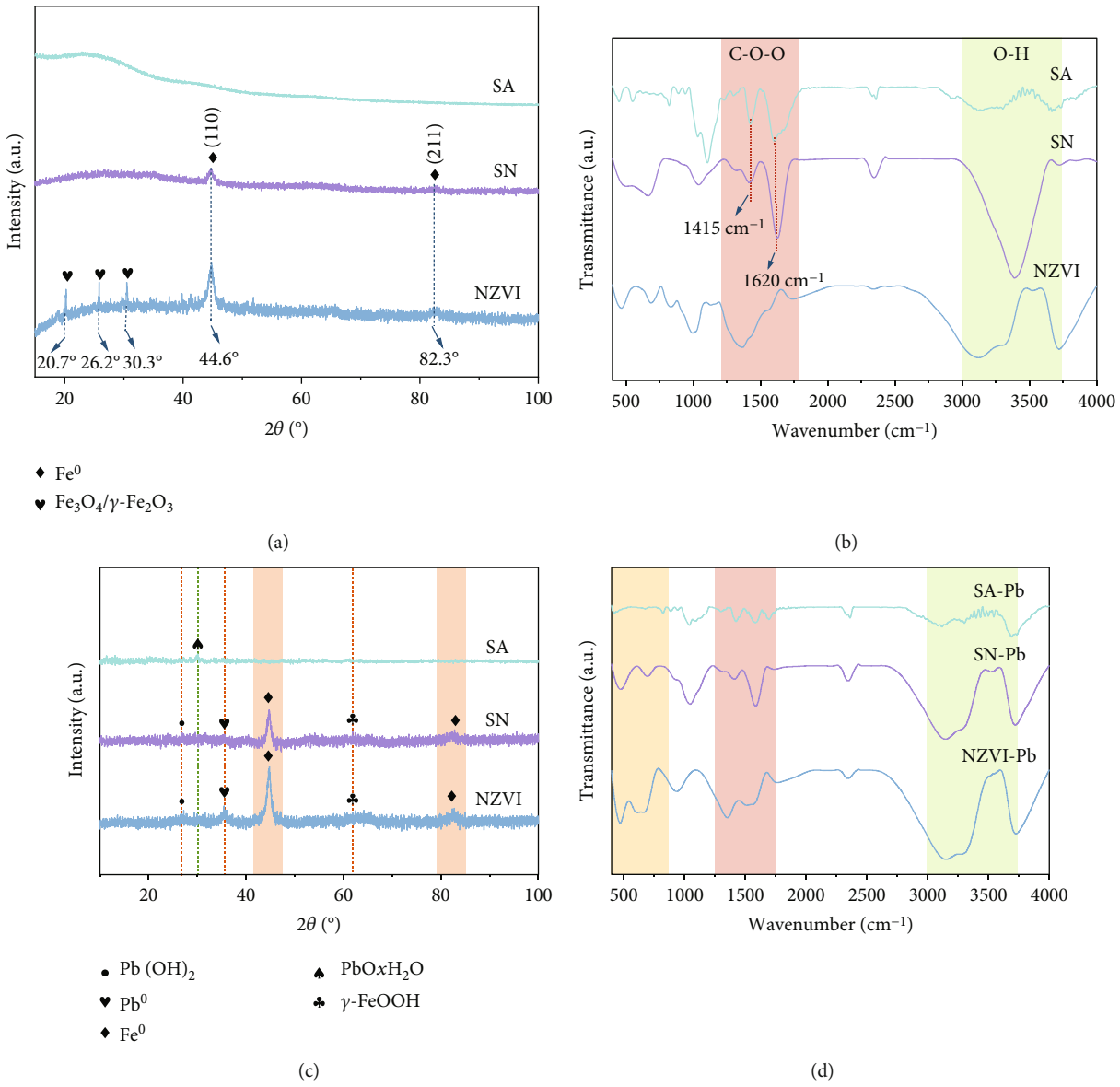

FIGURE 3: (a) XRD patterns of SN, NZVI, and SA; (b) FT-IR patterns of SN, NZVI, and SA; (c) XRD patterns, and (d) FT-IR patterns of SN, NZVI, and SA after the adsorption of Pb(II).

adsorption phase, corresponding to 0 to 30 min, 0 to 10 min, and 0 to 60 min for SN, NZVI, and SA, respectively, with the adsorption amounts (q_t) of Pb(II) of 4.93 mg/g, 4.81 mg/g, and 4.53 mg/g, respectively. The observed rapid adsorption of Pb(II) can be attributed to the abundance of active sites present on the surface of the material, which facilitate the efficient transfer of the pollutant from solution to the surface of the adsorbent [27, 28]. The second stage of Pb(II) adsorption by SN, NZVI, and SA was from 30 to 60 min, 10 to 60 min, and 60 to 150 min, respectively. q_t showed a slowly increasing trend with the extension of time and remained stable after 60 min to reach the adsorption equilibrium. The equilibrium adsorption amount (q_e) was 5 mg/g for both SN and NZVI and 4.56 mg/g for SA. In addition, the adsorption efficiencies of SN, NZVI, and SA for Pb(II) at 30 min were 98.7%, 99.3%, and 74.1%, respectively. The above results indicated that the adsorption capacity of SN and NZVI for Pb(II) was closer to each other and higher than that of SA.

The proposed first-order kinetic model and the proposed second-order kinetic model were developed, respectively, and the relevant parameters are shown in Table 1. The proposed second-order kinetic model had a better fit from the correlation coefficient R^2, which indicated that the adsorption of Pb(II) on SN, NZVI, and SA was mainly a chemisorption process, and chemical interaction such as electron sharing occurred between the adsorbent and the adsorbate [29]. In Figure 5, the $K_2 q_{e,cal}{}^2$ value of SN (mg/(g min)) was significantly higher than that of SA (0.40 mg/(g min)) and much lower than that of NZVI, which was ascribed to the higher reactivity of NZVI [30].

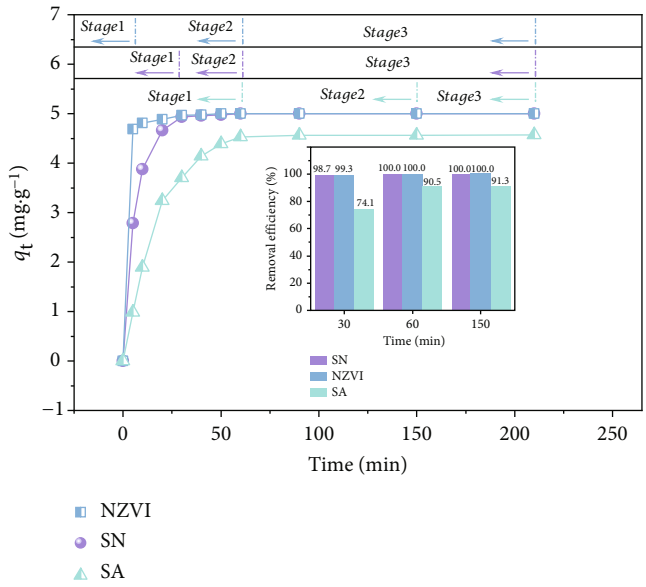

Figure 4: Adsorption of Pb(II) by SN, NZVI, and SA at different contact times.

Table 1: Adsorption kinetic parameters.

Models	Parameters	SN	NZVI	SA
Proposed first-order dynamics model	$q_{e,\exp}$ (mg/g)	5.00	5.00	4.56
	$q_{e,\mathrm{cal}}$ (mg/g)	3.50	1.29	7.12
	K_1 (1/min)	0.11	0.12	0.09
	R^2	0.96	0.88	0.97
Proposed second-order dynamics model	$q_{e,\exp}$ (mg/g)	5.00	5.00	4.56
	$q_{e,\mathrm{cal}}$ (mg/g)	5.36	5.04	5.12
	K_2 (g/(mg·min))	0.05	0.42	0.02
	R^2	1.00	1.00	0.99

Langmuir and Freundlich's adsorption isotherm models were developed (Figure 6). The maximum adsorption amounts of SN and NZVI for Pb(II) were 70.92 and 77.93 mg/g, respectively, which were much higher than those of SA. In Table 2, K_F (NZVI) = 38.41 > K_F (SN) = 32.80 > K_F (SA) = 3.79, and all n values were greater than 1, which was preferential adsorption [31]. In general, the adsorption performance of Pb(II) by alginate-coated NZVI has been greatly improved.

Figure 7 shows the reuse ability of SN and NZVI; the amount of adsorbent was 0.10 g in each cycle. After five cycles of adsorption, the removal rates of Pb(II) with the initial concentration of 10 mg/L by SN and NZVI were 99.99%, 97.28%, 96.98%, 95.76%, 95.11%, and 99.99%, 95.30%, 90.49%, 87.50%, and 79.13%, respectively. The results showed that SN particles exhibited a more stable processing efficiency than NZVI. Given the small size and reduced recyclability of NZVI particles, the efficacy of various adsorbents in removing Pb(II) was assessed upon factoring in mass loss. The removal rates of SN for Pb(II) were 99.99%, 94.67%, 93.90%, 91.89%, and 88.65%, while the corresponding removal rates of NZVI were 99.99%, 84.89%, 73.41%, 67.57%, and 64.53%, respectively. After five adsorption–desorption cycles, the maximum uptake capacity of Pb(II) by the SN was reduced from 5.00 to 4.43 mg/g. However, the maximum uptake capacity of NZVI decreased from 5.00 to 3.23 mg/g. This indicated that SN had better reusability and could be considered a promising material for the purification of lead-containing wastewater. And the cost estimates (Table 3) showed that SN is cost-effective for removing Pb(II) compared to NZVI and other iron-based materials.

The effects of SN and NZVI on the removal of Pb(II) at different aging times (0, 5, 10, 30, and 90 days) were investigated, and the results are shown in Figure 8. On the 90th day of aging, NZVI showed a significant decrease in lead removal efficiency, while SN remained at a high level (95.39%) (Figure 8(a)). Furthermore, as depicted in Figure 8(b), NZVI exhibited a more pronounced decrease in equilibrium adsorption capacity relative to SN, thereby suggesting that that SN had better antiaging properties than NZVI.

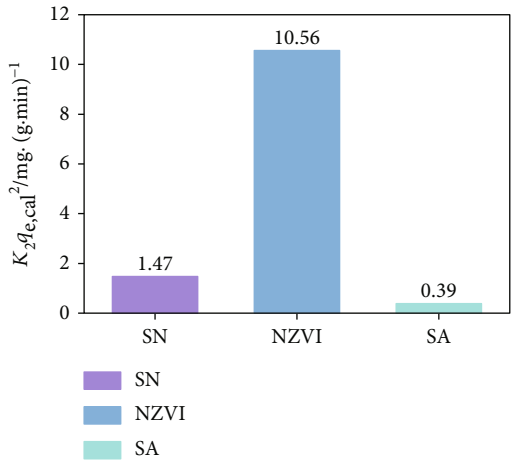

Figure 5: Initial adsorption rate constants for SN, NZVI, and SA.

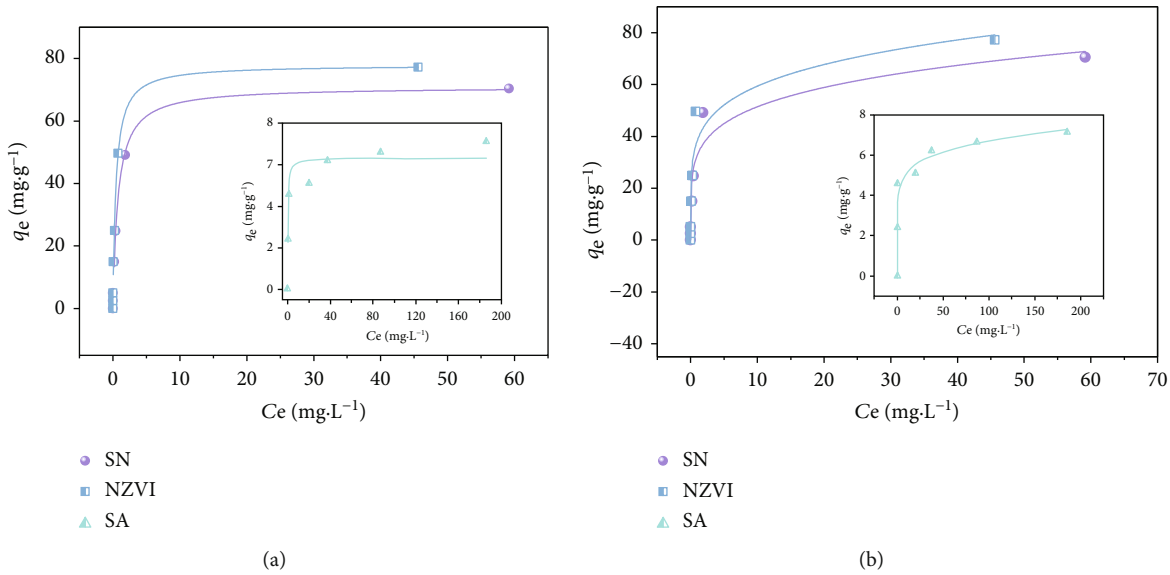

Figure 6: (a) Langmuir and (b) Freundlich adsorption isotherm models for SN, NZVI, and SA.

The XRD and FT-IR patterns of SN, NZVI, and SA after treatment with Pb(II) are given in Figure 3. The characteristic diffraction peaks attributed to Fe^0 (α-Fe^0(110) crystal plane and α-Fe^0(211) crystal plane) at $2\theta = 44.6^\circ$ and 82.3° were observed for both SN and NZVI, indicating that Fe^0 was still present in the degradation products [34]. The diffraction peaks at $2\theta = 26.9^\circ$ and 35.7° for SN and NZVI were attributed to $Pb(OH)_2$ and Pb^0, respectively [35, 36]. In addition, a new characteristic peak corresponding to the (202) crystal plane of $PbO{\bullet}xH_2O$ appeared at $2\theta = 29.3^\circ$ for SA [36]. Absorption bands associated with antisymmetric, symmetric stretching vibrations of carboxyl functional groups were present in the range of 1400-1650 cm^{-1} for SN and SA and shifted from 1626 cm^{-1}, 1415 cm^{-1} to 1583 cm^{-1}, 1412 cm^{-1} for SN and from 1619 cm^{-1}, 1423 cm^{-1} to 1579 cm^{-1}, 1419 cm^{-1} for SA compared to preadsorption. The change in the vibrational position of the carboxyl functional group suggested that the C-O-O functional group in SN and SA might be engaged in the removal of Pb(II) through complexation. The new absorption band of SN at 3723 cm^{-1} was attributed to the stretching motion of the metal hydroxide O-H and the formation of $Pb(OH)_2$.

The mechanism of Pb(II) adsorption by SN was probed using XPS spectroscopy (Figure 9). The full scan mode results showed the presence of Pb in the SN-Pb(II) complex, demonstrating the absorption of Pb(II) on the SN surface (Figure 9(a)). The high-resolution spectra of the C1s of SN particles before adsorption are shown in Figure 9(b), where the peaks corresponding to 284.8, 286.4, and 288.7 eV were attributed to C-C, C-O, and C=O bonds, respectively [37]. And the C-O and C=O corresponding to SN after adsorption of Pb(II) binding energy shifted after the adsorption of Pb(II), indicating that the C-O and C=O groups on the

Table 2: Parameters of SN, NZVI, and SA adsorption isotherm models.

Models	Parameters	SN	NZVI	SA
Langmuir	q_m (mg/g)	70.92	77.93	6.31
	K_L (mg/g)	1.31	2.24	3.02
	R^2	1.00	0.99	0.86
Freundlich	K_F mg/$\left(\mathrm{L}^{(1-1/n)} \cdot \mathrm{g}\right)$	32.80	38.41	3.79
	n	5.13	5.29	8.12
	R^2	0.94	0.94	0.96

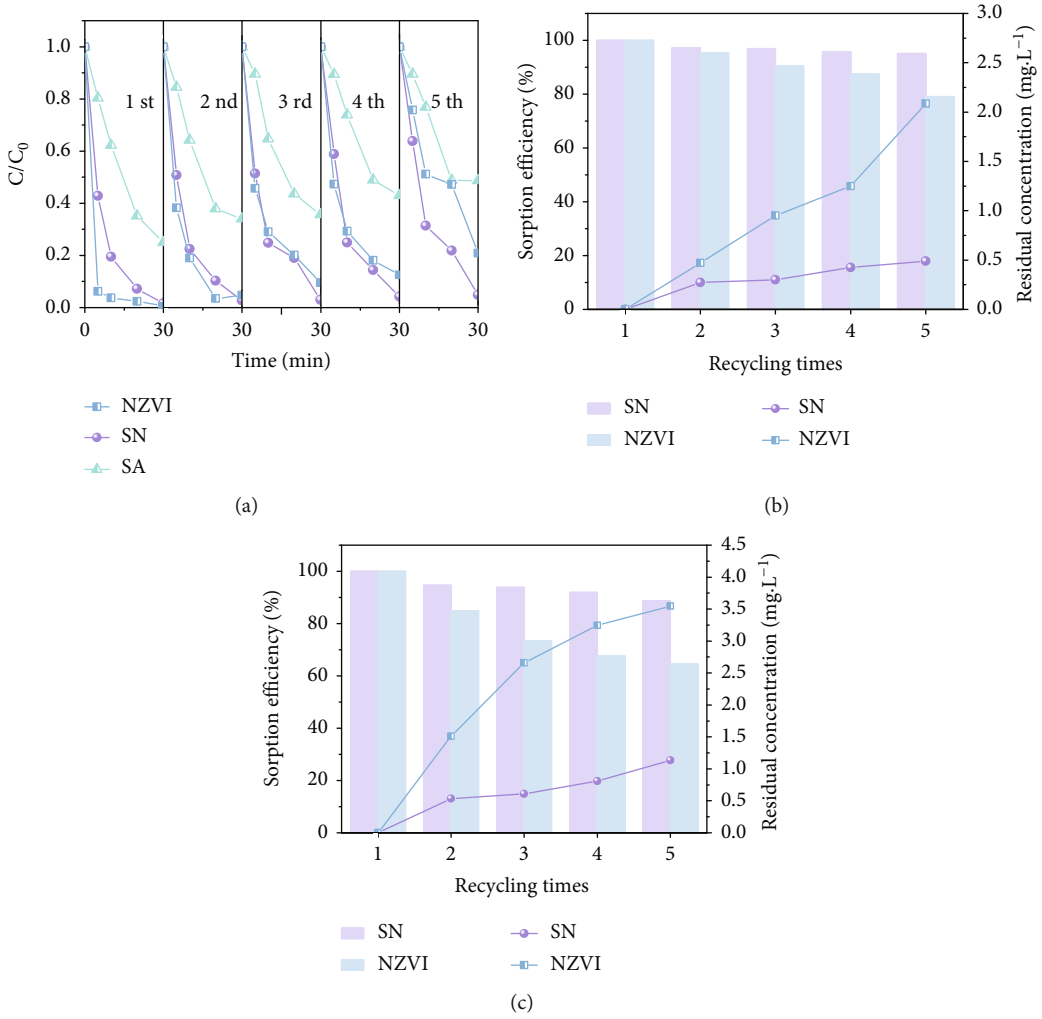

Figure 7: (a) Cyclic adsorption capacity of SN, NZVI, and SA. (b) Removal of lead by equal amounts of SN and NZVI. (c) Removal of lead by SN and NZVI after considering mass loss.

surface of SN were involved in the removal of Pb(II). Figure 9(c) shows the high-resolution spectra of the O1s region before and after the adsorption of Pb(II) by SN. The peaks at 531.76, 533.29, and 529.84 eV of SN before adsorption were attributed to -OH, C-O, and Fe-O [38, 39], respectively, indicating the presence of oxygen-containing functional groups on the surface of SN. After the adsorption of Pb(II), the peak positions of O1s were found to be shifted to the positions of 531.79, 533.27, and 529.86 eV, while the contents of the corresponding functional groups -OH, C-O, and Fe-O changed from 52.41%, 44.04%, and 3.55% to 48.75%, 45.51%, and 5.74%, respectively. This indicated that the removal of Pb(II) was facilitated by the oxygen-containing functional groups present on SN, mainly

Table 3: The reagent consumption and cost for synthesizing 1 kg of material.

Samples	NZVI	SN	A-nZVI	S-nZVI
$FeCl_3{\cdot}6H_2O$ (kg)	4.88	2.93	3.93	4.38
$NaBH_4$ (kg)	3.50	2.10	3.33	3.72
SA (kg)	—	0.40	—	—
$CaCl_2$ (kg)	—	3.20	—	—
EDA (L)	—	—	3.00	—
$Na_2S_2O_4$ (kg)	—	—	—	0.44
Total (RMB)	8397	5079	9486	7570
References	This work	This work	[32]	[33]

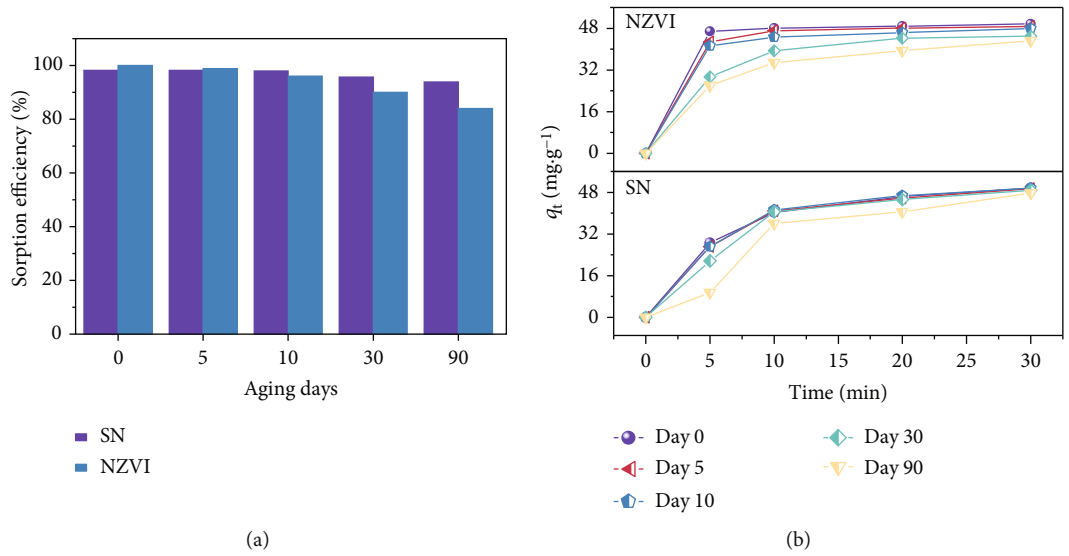

Figure 8: (a) Removal efficiency and (b) adsorption capacity of SN and NZVI for Pb(II) after different times of aging.

including the ion exchange between hydroxyl/carboxyl groups and Pb(II). The change in the iron-oxygen bonding also indicated the involvement of Fe^0 and its oxides encapsulated in SN in the removal of Pb(II) through redox processes. In Figure 9(d), the peaks of SN at binding energies of 705.2 (718.2), 710.5 (723.6), and 712.2 (725.3) eV corresponded to Fe^0, Fe (II), and Fe (III), respectively, and the percentage of their peak areas changed from 36.49%, 20.75%, and 45.28% before adsorption to 23.19%, 27.54%, and 40.27%, which was attributed to the occurrence of redox reactions. Figure 9(e) shows the Pb 4f region of SN after adsorption. The peaks at 139.7 eV and 143.9 eV corresponded to Pb(II) in Pb $(NO_3)_2$ [40]. The characteristic peaks that remained unchanged correspond to free Pb(II) adsorbed through physical mechanisms, such as electrostatic forces, which were not bonded to the material surface. After the adsorption of Pb(II), the main peaks of Pb $4f_{7/2}$ and Pb $4f_{5/2}$ in SN were detected at 138.4 and 143.4 eV, respectively. The binding energy of Pb $4f_{7/2}$ and Pb $4f_{5/2}$ shifted in the negative direction compared to 139.7 eV and 143.9 eV in $Pb(NO_3)_2$, indicating that the atoms gain electrons [40]. In general, the removal of Pb(II) by SN involved ion exchange. The -COOH and -COONa groups on the surface of SN provided lone pair electrons, while Pb^{2+} and $Pb(OH)^+$ ions provide empty orbitals. The binding energy of the Pb element shifted to low energy due to the electron gain of the empty Pb orbital. In addition, the peak observed at 138.4 eV was consistent with the peak of $Pb(OH)_2$, indicating that Pb(II) might interact with OH^- generated by the oxidation of NZVI and be removed by coprecipitation.

Moreover, the pH of the solution affects both the speciation of Pb and the surface charge density of the material, which is considered to be an important factor in the adsorption process of Pb(II) [41]. Figure 9(f) shows the speciation of Pb at various pH values. It was found that at pH <5.0, Pb was mainly in the form of Pb(II). $Pb(OH)^+$ began to appear when pH >5.0. Notably, $Pb(OH)_2$ precipitates might form at pH >7.0. Therefore, in order not to interfere with the effect of the study material on Pb(II) adsorption, an upper limit of pH = 5.0 was set for this study.

Figure 9(g) shows the equilibrium adsorption capacity and zeta potential of SN for Pb(II) at varying pH levels. Notably, the results demonstrate that pH exerted a significant impact on the adsorption capacity. When pH = 1.0,

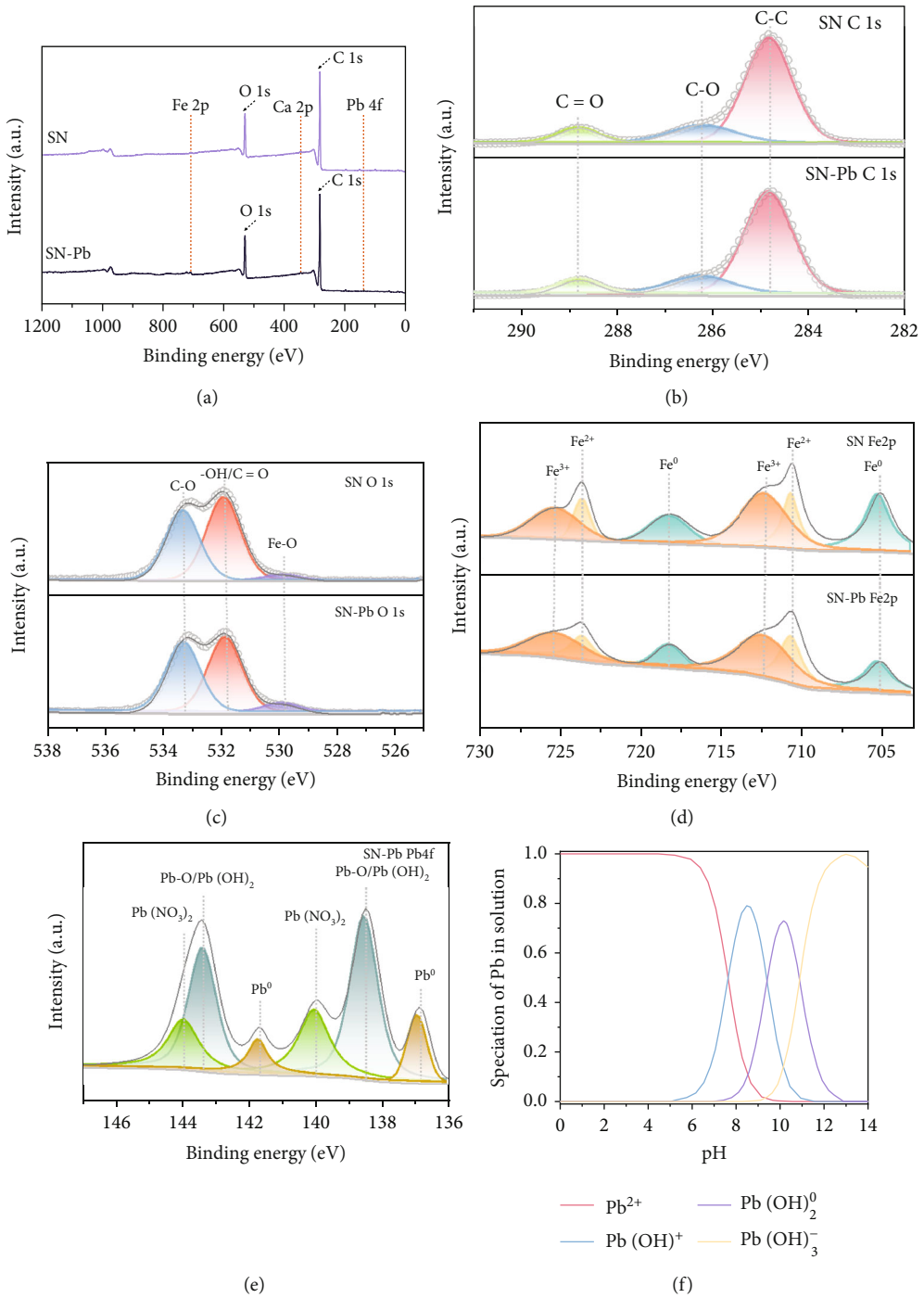

Figure 9: Continued.

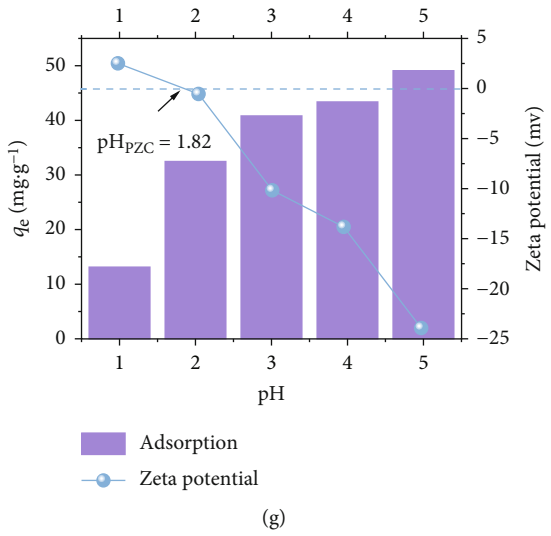

(g)

Figure 9: High-resolution spectra of (a) XPS total spectrum, (b) C 1 s, (c) O 1 s, (d) Fe 2p, (e) Pb 4f before and after Pb(II) adsorption by SN, (f) speciation distribution of Pb at different pH, and (g) equilibrium adsorption capacity of SN and zeta potential of SN at different pH.

the adsorption rate of SN was relatively low, which might be due to the fact that at a relatively low pH of the solution, the surface of SN was positively charged, which would mutually repel Pb(II) in the solution and hinder the adsorption of Pb(II). At the same time, the large amount of H^+ in the water might compete with Pb(II) for the redox site of zero-valent iron and the functional groups such as carboxyl in alginate, thus reducing the removal rate of Pb(II) [42]. With the increase in pH, when the pH exceeded pH$_{PZC}$ (1.82), especially pH = 5.0, SN had the largest adsorption capacity of Pb(II) (49.09 mg/g). At this time, there was a negative charge on the surface of SN, and the electrostatic attraction provided a strong driving force for the rapid adsorption of Pb(II) [43].

Therefore, the removal of Pb(II) by SN involved the synergistic effects of various mechanisms such as electrostatic interaction, redox, ion exchange, and coprecipitation. The main reactions to this process were as follows:

$$\begin{aligned}
Fe + 2H_2O &\longrightarrow Fe^{2+} + H_2\uparrow + 2OH^-,\\
Pb^{2+} + 2OH^- &\longrightarrow Pb(OH)_2\downarrow,\\
Pb^{2+} + Fe &\longrightarrow Pb^0 + Fe^{2+},\\
Pb^{2+} + 2Fe^{2+} &\longrightarrow Pb^0 + 2Fe^{3+},\\
2Fe^{2+} + 2H_2O &\longrightarrow 2Fe^{3+} + H_2\uparrow + 2OH^-,\\
Fe^{3+} + 3OH^- &\longrightarrow FeOOH + H_2O,\\
2FeOOH &\longrightarrow Fe_2O_3\downarrow + H_2O,\\
2Fe^{3+} + Fe^{2+} + 8OH^- &\longrightarrow Fe_3O_4\downarrow + 4H_2O,\\
\equiv C - OH + Pb^{2+} &\longrightarrow \equiv C - O - Pb^+ + H^+,\\
R - COO(H, Ca) + Pb^{2+} &\longrightarrow (R - COO)_2Pb + 2H^+, Ca^{2+}.
\end{aligned} \tag{8}$$

In summary, the mechanism of Pb(II) removal by SN could be divided into two aspects (Figure 10), attributed to the unique

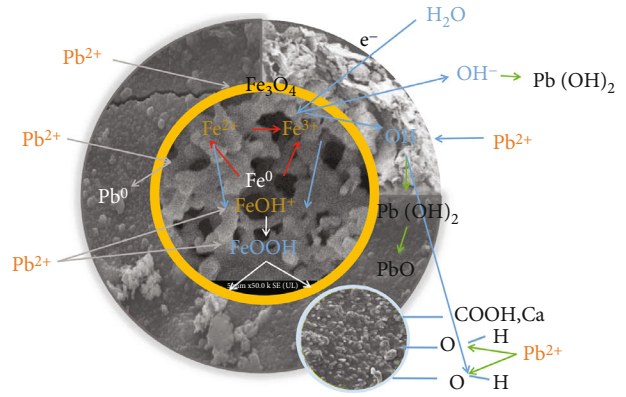

Figure 10: Schematic diagram of the mechanism of lead removal by SN.

action of NZVI on the one hand: (1) the diffusion of Pb(II) in solution to the surface of NZVI wrapped by SN under the adsorption of alginate and NZVI particles; (2) the immobilization of Pb(II) on the surface of NZVI by adsorption and precipitation, and the direct or indirect reduction on the surface of NZVI and oxides (such as Fe_2O_3, Fe_3O_4, and Fe(OOH)) were formed on the surface of NZVI; and (3) Pb(II) was converted to Pb(OH)$_2$. On the other hand, it was mainly due to the role of functional groups such as -OH/-COO(H, Ca) contained on the surface of SN in the adsorption of Pb(II), and the interaction between Pb(II) and -OH/-COO(H, Ca) ion exchange interactions, leading to the formation of inner-sphere complexes. In addition, the pore-filling effect was also thought to be involved in the adsorption process of Pb(II).

To investigate the influence of aging on the composition of the adsorbent, XRD analysis was performed on NZVI and SN after aging for different days (Figures 11(a) and 11(b)). Diffraction peaks at 2θ=44.6° and 2θ=82.3° for SN and NZVI have been attributed to the α-Fe^0(110) and α-Fe^0(211) crystal planes of the zero-valent iron body-centered cubic structure, respectively [34]. After 30 days of

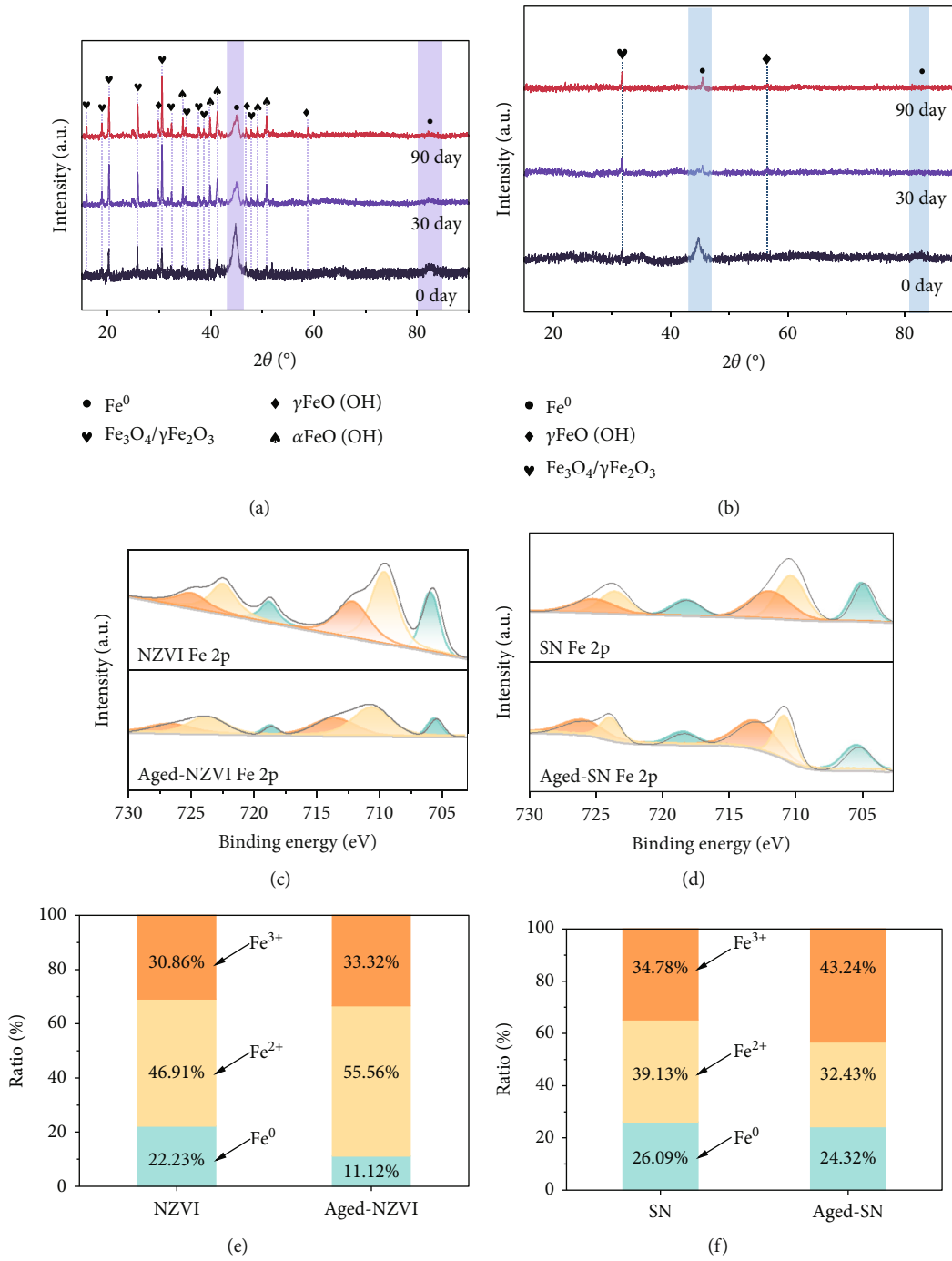

FIGURE 11: (a) XRD patterns of NZVI before and after aging; (b) XRD patterns of SN before and after aging; (c) Fe 2p high resolution spectra of NZVI; (d) Fe 2p high resolution spectra of SN; (e) Fe valence distribution in NZVI; (f) Fe valence distribution in SN.

aging, NZVI showed diffraction peaks belonging to magnetite (Fe_3O_4) or maghemite (γFe_2O_3) at 2θ=16.6°, 18.4°, 20.7°, 26.2°, 30.3°, 32.2°, 35.7°, 37.3°, 38.9°, and 47.1°, and SN showed diffraction peaks belonging to maghemite (γFe_2O_3) at 2θ=32.2° [44]. The diffraction peak of SN at 56.6° and the small diffraction peaks of NZVI at 2θ=29.9°, 46.6°, and 59.0° belonged to lepidocrocite (γFeO(OH)). In addition, the diffraction peaks of NZVI at 2θ=34.7°, 39.9°, 41.2°, 49.8°, and 50.6° belonged to goethite (αFeO(OH)) [45]. The conversion of the material to iron hydroxide during aging could be attributed to the following reactions: Fe^{2+} was first formed on the surface of the material and rapidly oxidized to Fe^{3+}, and then Fe^{3+} reacted with hydroxyl groups, with the following main reactions occurring [44]:

$$\begin{aligned} Fe^0 + 2H_2O &\longrightarrow Fe^{2+} + H_2\uparrow + 2OH^-, \\ 6Fe^{2+} + O_2 + 6H_2O &\longrightarrow 2Fe_3O_4(S) + 12H^+, \\ 4Fe^0 + 3O_2 + 2H_2O &\longrightarrow 4FeO(OH), \end{aligned} \tag{9}$$

After aging for 90 days, γFeO(OH) and $Fe_3O_4/\gamma Fe_2O_3$ were the dominant components in both SN and NZVI, apart from zero-valent iron, while a small amount of needle ferrite was present in NZVI. XRD peak intensity of γFeO(OH) and $Fe_3O_4/\gamma Fe_2O_3$ in NZVI increased significantly with the increase in sitting time, indicating that the crystallinity of corrosion products increased [44]. It was observed that the type of corrosion product species generated by SN was conspicuously lesser than that of NZVI, suggesting a plausible influence of the wrapping material on Fe conversion. The diffraction peak intensities of γFeO(OH) and $Fe_3O_4/\gamma Fe_2O_3$ did not change significantly after 30 days of aging of SN and 90 days of aging, but the intensity of the related diffraction peak in NZVI was significantly enhanced, indicating that the wrapping might slow down the Fe^0 passivation rate.

In Figure 11, it could be seen from the high-resolution spectra of NZVI and SN in the Fe 2p region before and after aging that there were three kinds of iron (Fe^0, Fe (II), and Fe (III)) on the surface of the material, and the corresponding binding energies were 705.2 (718.2), 710.5 (723.6), and 712.2 (725.3) eV, respectively. It could be seen that the Fe^0 peak of NZVI gradually decreased with the increase in aging time and decreased to 11.11% at 90 days of aging, while the Fe^0 content in SN only decreased to 24.32%. The contents of Fe (II) and Fe (III) in NZVI and SN after aging were 55.56%, 33.33%, and 32.43%, 43.24%, respectively. Combined with the results of XRD and XPS, it could be seen that the decrease in the reactivity of NZVI to Pb(II) should be attributed to the formation of the surface oxide layer, which hindered the electron transfer and reduced the adsorption rate and removal rate of NZVI to Pb(II). SN exhibited better anti-aging performance. On the one hand, the surface shell slowed down the oxidation of zero-valent iron in the air. On the other hand, the removal of Pb(II) by SN involved various synergistic effects such as electrostatic interaction, redox, ion exchange, and coprecipitation. When the formation of a surface oxide layer hindered the transfer of electrons, these reaction processes still stabilized the adsorption capacity of SN.

4. Conclusion

Herein, we successfully prepared SN by SA wrapping with NZVI as the core for the removal of Pb(II) from the solution. SEM-EDS and BET analyses showed that there was abundant pore distribution inside the NZVI spheres, and the specific surface area of SN reached 47.05 m^2/g, indicating that the wrapping could significantly improve the agglomeration of NZVI. Moreover, the characterization results of XRD and FT-IR proved that the SA wrapping effectively inhibited the formation of oxides on the surface of NZVI while simultaneously introducing functional groups such as C-O, COO-, and O-H onto the SN surface. The performance test results showed that the maximum adsorption of SN on Pb(II) was 70.92 mg/g when the pH = 5 of the solution. The proposed second-order kinetic model and the Langmuir model described the elimination of Pb(II) better. The thermodynamically fitted data indicated that the removal of Pb(II) was a chemisorption reaction that proceeded spontaneously. In addition, the removal mechanism of Pb(II) by SN was characterized by XRD, FT-IR, and XPS. It was found that Pb(II) was converted to Pb^0 during the reaction, and Pb(II) in solution would be removed by direct precipitation between the hydroxyl groups produced by the oxidation of Fe^0 to form $Pb(OH)_2$. Finally, the stability of SN was evaluated, and it was found that the percentage of Fe^0 content only decreased from 26.09% to 24.32% after aging SN in the air for 90 days, and the main products of oxidation were $Fe_3O_4/\gamma Fe_2O_3$ and γFeO(OH). Overall, this study shows that SN proves to be a potential adsorbent for the efficient removal of heavy metals from wastewater.

Data Availability

Data will be made available on request.

Conflicts of Interest

No potential conflict of interest was reported by the authors.

Authors' Contributions

Chunli Zheng did the conceptualization, data analysis, supervision, and writing which is the review and editing. Jieling Ren performed the methodology, investigation, data curation, visualization, and writing the original draft, review and editing. Fei He did the writing which is the review and editing. Yingying Yong did the writing which is the review and editing. Yanhong Tu did the review and editing. Zhenxing Wang conducted the conceptualization and funding acquisition.

Acknowledgments

This work was funded by the National Key Research and Development Project (2019YFC1804800), the Science and Technology Program of Guangdong Forestry Administration (2020-KYXM-08), the Science and Technology Program of Jinhua (2022-4-042), and the Youth Foundation of SCIES (PM-zx097-202304-147).

References

[1] Q. Y. Ma, T. J. Logan, and S. J. Traina, "Lead immobilization from aqueous solutions and contaminated soils using phosphate rocks," *Environmental Science & Technology*, vol. 29, no. 4, pp. 1118–1126, 1995.

[2] J. Kaushik, T. K. M. Gunture, R. Singh, and S. K. Sonkar, "Thiourea-functionalized graphene aerogel for the aqueous phase sensing of toxic Pb(II) metal ions and H_2O_2," *Chemosphere*, vol. 287, Part 2, article 132105, 2022.

[3] L. Castro, M. L. Blázquez, F. González, J. A. Muñoz, and A. Ballester, "Heavy metal adsorption using biogenic iron compounds," *Hydrometallurgy*, vol. 179, pp. 44–51, 2018.

[4] H. Y. Wu, W. J. Wang, Y. F. Huang et al., "Comprehensive evaluation on a prospective precipitation-flotation process for metal-ions removal from wastewater simulants," *Journal of Hazardous Materials*, vol. 371, pp. 592–602, 2019.

[5] R. M. Ashour, R. El-sayed, A. F. Abdel-Magied et al., "Selective separation of rare earth ions from aqueous solution using functionalized magnetite nanoparticles: kinetic and thermodynamic studies," *Chemical Engineering Journal*, vol. 327, pp. 286–296, 2017.

[6] R. M. Ashour, H. N. Abdelhamid, A. F. Abdel-Magied, and A. A. Abdel-khalek, "Rare earth ions adsorption onto graphene oxide nanosheets," *Solvent Extraction and Ion Exchange*, vol. 35, no. 2, pp. 91–103, 2017.

[7] T. T. Yang, Y. M. Xu, Q. Q. Huang et al., "An efficient biochar synthesized by iron-zinc modified corn straw for simultaneously immobilization Cd in acidic and alkaline soils," *Environmental Pollution*, vol. 291, article 118129, 2021.

[8] W. Y. Ma, T. Sun, Y. M. Xu, S. N. Zheng, and Y. B. Sun, "In – situ immobilization remediation, soil aggregate distribution, and microbial community composition in weakly alkaline Cd–contaminated soils: a field study," *Environmental Pollution*, vol. 292, article 118327, 2022.

[9] Y. Xu, X. F. Liang, Y. M. Xu et al., "Remediation of heavy metal-polluted agricultural soils using clay minerals: a review," *Pedosphere*, vol. 27, no. 2, pp. 193–204, 2017.

[10] R. Gruter, B. Costerousse, J. Mayer et al., "Long-term organic matter application reduces cadmium but not zinc concentrations in wheat," *Science of The Total Environment*, vol. 669, pp. 608–620, 2019.

[11] Y. M. Zhou, B. Gao, A. R. Zimmerman, and X. D. Cao, "Biochar-supported zerovalent iron reclaims silver from aqueous solution to form antimicrobial nanocomposite," *Chemosphere*, vol. 117, pp. 801–805, 2014.

[12] S. S. Wang, B. Gao, Y. C. Li, A. E. Creamer, and F. He, "Adsorptive removal of arsenate from aqueous solutions by biochar supported zero-valent iron nanocomposite: batch and continuous flow tests," *Journal of Hazardous Materials*, vol. 322, pp. 172–181, 2017.

[13] X. Li, L. Ai, and J. Jiang, "Nanoscale zerovalent iron decorated on graphene nanosheets for Cr(VI) removal from aqueous solution: surface corrosion retard induced the enhanced performance," *Chemical Engineering Journal*, vol. 288, pp. 789–797, 2016.

[14] Y. Xie and D. M. Cwiertny, "Use of dithionite to extend the reactive lifetime of nanoscale zero-valent iron treatment systems," *Environmental Science & Technology*, vol. 44, no. 22, pp. 8649–8655, 2010.

[15] K. M. Gopi, K. Pakshirajan, and G. Das, "Heavy metal removal from aqueous solution using sodium alginate immobilized sulfate reducing bacteria: mechanism and process optimization," *Journal of Environmental Management*, vol. 218, pp. 486–496, 2018.

[16] H. X. Ren, Z. M. Gao, D. J. Wu, J. H. Jiang, Y. M. Sun, and C. W. Luo, "Efficient Pb(II) removal using sodium alginate-carboxymethyl cellulose gel beads: preparation, characterization, and adsorption mechanism," *Carbohydrate Polymers*, vol. 137, pp. 402–409, 2016.

[17] H. Hecht and S. Srebnik, "Structural characterization of sodium alginate and calcium alginate," *Biomacromolecules*, vol. 17, no. 6, pp. 2160–2167, 2016.

[18] Z. Yu, H. J. Li, L. M. Zhang, Z. H. Zhu, and L. Q. Yang, "Enhancement of phototoxicity against human pancreatic cancer cells with photosensitizer-encapsulated amphiphilic sodium alginate derivative nanoparticles," *International Journal of Pharmaceutics*, vol. 473, no. 1-2, pp. 501–509, 2014.

[19] Z. H. Li, S. Y. Xu, G. H. Xiao, L. M. Qian, and Y. Song, "Removal of hexavalent chromium from groundwater using sodium alginate dispersed nano zero-valent iron," *Journal of Environmental Management*, vol. 244, pp. 33–39, 2019.

[20] S. K. Lakkaboyana, S. Khantong, N. K. Asmel et al., "Indonesian kaolin supported nZVI (IK-nZVI) used for the an efficient removal of Pb(II) from aqueous solutions: kinetics, thermodynamics and mechanism," *Journal of Environmental Chemical Engineering*, vol. 9, no. 6, article 106483, 2021.

[21] W. Wang, Y. L. Hua, S. L. Li, W. L. Yan, and W. X. Zhang, "Removal of Pb(II) and Zn(II) using lime and nanoscale zero-valent iron (nZVI): a comparative study," *Chemical Engineering Journal*, vol. 304, pp. 79–88, 2016.

[22] J. Liu, V. Makwana, J. Cai, S. L. Suib, and M. Aindow, "Effects of alkali metal and ammonium cation templates on nanofibrous cryptomelane-type manganese oxide octahedral molecular sieves (OMS-2)," *The Journal of Physical Chemistry. B*, vol. 107, no. 35, pp. 9185–9194, 2003.

[23] E. P. Barrett, L. G. Joyner, and P. P. Halenda, "The determination of pore volume and area distributions in porous substances. I. Computations from nitrogen isotherms," *Journal of the American Chemical Society*, vol. 73, no. 1, pp. 373–380, 1951.

[24] K. Piechocki, M. Kozanecki, and J. Saramak, "Water structure and hydration of polymer network in $PMEO_2MA$ hydrogels," *Polymer*, vol. 210, article 122974, 2020.

[25] M. Y. Zhang, K. X. Yi, X. W. Zhang, P. Han, W. Liu, and M. P. Tong, "Modification of zero valent iron nanoparticles by sodium alginate and bentonite: enhanced transport, effective hexavalent chromium removal and reduced bacterial toxicity," *Journal of Hazardous Materials*, vol. 388, article 121822, 2020.

[26] A. Bajpai, "Facile preparation of ionotropically crosslinked chitosan-alginate nanosorbents by water-in-oil (W/O) microemulsion technique: optimization and study of arsenic (V) removal," *Journal of Water Process Engineering*, vol. 32, article 100920, 2019.

[27] J. L. Dai, M. Zhang, Q. H. Hu, Y. Z. Huang, R. Q. Wang, and Y. G. Zhu, "Adsorption and desorption of iodine by various Chinese soils: II. Iodide and iodate," *Geoderma*, vol. 153, no. 1-2, pp. 130–135, 2009.

[28] Y. Zhang, Y. Wang, X. Zhang et al., "Investigating the behavior of binding properties between dissolved organic matter (DOM) and Pb (II) during the soil sorption process using parallel factor analysis (PARAFAC) and two-dimensional correlation spectroscopy (2D-COS)," *Environmental Science and Pollution Research*, vol. 24, no. 32, pp. 25156–25165, 2017.

[29] C. L. Zheng, S. S. Feng, P. P. Liu et al., "Sorption of organophosphate flame retardants on Pahokee peat soil," *Clean–Soil, Air, Water.*, vol. 44, no. 9, pp. 1163–1173, 2016.

[30] H. N. Tran, S. J. You, A. Hosseini-Bandegharaei, and H. P. Chao, "Mistakes and inconsistencies regarding adsorption of contaminants from aqueous solutions: a critical review," *Water Research*, vol. 120, pp. 88–116, 2017.

[31] W. R. Chen, X. K. Li, Z. Q. Pan, Y. X. Bao, S. S. Ma, and L. S. Li, "Efficient adsorption of norfloxacin by Fe-MCM-41 molecular sieves: kinetic, isotherm and thermodynamic studies," *Chemical Engineering Journal*, vol. 281, pp. 397–403, 2015.

[32] Q. Cheng, Q. R. Li, X. J. Huang et al., "The high efficient Sb(III) removal by cauliflower like amorphous nanoscale zero-valent iron (A-nZVI)," *Journal of Hazardous Materials*, vol. 436, article 129056, 2022.

[33] I. G. Song, Y. G. Kang, J. H. Kim, H. Yoon, W. Y. Um, and Y. S. Chang, "Assessment of sulfidated nanoscale zerovalent iron for _in-situ_ remediation of cadmium-contaminated acidic groundwater at a zinc smelter," *Journal of Hazardous Materials*, vol. 441, article 129915, 2023.

[34] X. Liu, D. Lai, and Y. Wang, "Performance of Pb(II) removal by an activated carbon supported nanoscale zero- valent iron composite at ultralow iron content," *Journal of Hazardous Materials*, vol. 361, pp. 37–48, 2019.

[35] M. Arshadi, M. Soleymanzadeh, J. W. L. Salvacion, and F. SalimiVahid, "Nanoscale Zero-valent Iron (NZVI) supported on _sineguelas_ waste for Pb(II) removal from aqueous solution: Kinetics, thermodynamic and mechanism," *Journal of Colloid and Interface Science*, vol. 426, pp. 241–251, 2014.

[36] Y. L. Shi, C. J. Yu, M. Y. Liu et al., "One-pot synthesis of spherical nanoscale zero-valent iron/biochar composites for efficient removal of Pb(ii)," *RSC Advances*, vol. 11, no. 58, pp. 36826–36835, 2021.

[37] X. N. Zhang, X. Y. Lin, Y. He, Y. Chen, X. G. Luo, and R. Shang, "Study on adsorption of tetracycline by cu-immobilized alginate adsorbent from water environment," *International Journal of Biological Macromolecules*, vol. 124, pp. 418–428, 2019.

[38] D. Li, Y. Zhong, H. L. Wang, W. L. Huang, and P. A. Peng, "Remarkable promotion in particle dispersion and electron transfer capacity of sulfidated nano zerovalent iron by coating alginate polymer," *Science of The Total Environment*, vol. 759, article 143481, 2021.

[39] Y. Hu, X. Peng, Z. H. Ai, F. L. Jia, and L. Z. Zhang, "Liquid nitrogen activation of zero-valent iron and its enhanced Cr(VI) removal performance," *Environmental Science & Technology*, vol. 53, no. 14, pp. 8333–8341, 2019.

[40] B. L. Zhang, W. Qiu, P. P. Wang et al., "Mechanism study about the adsorption of Pb(II) and Cd(II) with iron-trimesic metal-organic frameworks," vol. 385, Article ID 123507, 2020.

[41] S. Khan, M. Idrees, and M. Bilal, "Revealing and elucidating chemical speciation mechanisms for lead and nickel adsorption on zeolite in aqueous solutions," *Colloids and Surfaces A: Physicochemical and Engineering Aspects*, vol. 623, article 126711, 2021.

[42] J. Zhu, V. Cozzolino, M. Pigna, Q. Huang, A. G. Caporale, and A. Violante, "Sorption of cu, Pb and Cr on Na-montmorillonite: competition and effect of major elements," *Chemosphere*, vol. 84, no. 4, pp. 484–489, 2011.

[43] X. Zhang, S. Lin, X. Q. Lu, and Z. L. Chen, "Removal of Pb(II) from water using synthesized kaolin supported nanoscale zero-valent iron," *Chemical Engineering Journal*, vol. 163, no. 3, pp. 243–248, 2010.

[44] A. Liu, J. Liu, W. X. Zhang, and W. X. Zhang, "Transformation and composition evolution of nanoscale zero valent iron (nZVI) synthesized by borohydride reduction in static water," *Chemosphere*, vol. 119, pp. 1068–1074, 2015.

[45] A. R. Liu, J. Liu, J.,. H. Han, and W. X. Zhang, "Evolution of nanoscale zero-valent iron (nZVI) in water: microscopic and spectroscopic evidence on the formation of nano- and microstructured iron oxides," *Journal of Hazardous Materials*, vol. 322, no. Part A, pp. 129–135, 2017.